nature sensors

Article

https://doi.org/10.1038/s44460-026-00091-7

Elastic in vivo biosignal amplifiers based on strain-insensitive material and circuit design

Received: 15 May 2025

Accepted: 20 May 2026

Published online: 30 July 2026

Check for updates

Wenxi Sun (孙文熙)[1,2], Xiran Pan (潘熙然)[1], Wanqiong Yuan (原婉琼)[3,4,5], Weiwei Xia (夏威威)[6], Xun Lei (雷洵)[1], Peiyun Li (李佩雲)[1], Chengyu Wang (王程昱)[1], Biqin Yang (杨必勤)[1], Yuting Zheng (郑宇婷)[1], Xiao-Yan Zhang (章笑研)[7], Simin Liang (梁思敏)[1], Xiu Wang (王秀)[1], Bingqi Wang (王炳琦)[1], Yuying Wu (吴俞营)[1], Pan Gu (谷攀)[1], Kai Liu (刘凯)[1], Hanqiang Ouyang (欧阳汉强)[3,4,5], Chenxin Zhu (朱晨昕)[8], Zhi Zhang (张志)[1] ✉ & Ting Lei (雷霆)[1] ✉

Biological tissues undergo continuous, heterogeneous deformation, so that implantable biosensors must be soft, elastic and operationally stable in aqueous environments. Weak physiological signals are distorted at the biotic/abiotic interface, making in situ amplification essential for high-fidelity recording, yet existing devices cannot simultaneously provide strain-insensitive operation, aqueous stability and amplification. Here we introduce an integrated material–device–circuit strategy that enables the fabrication of elastic organic electrochemical transistor amplifiers with stable in vivo performance, including: a stretchable, aqueous-stable n-type polymer, P(bgTDPP-TVT-CN2) that maintains high performance under 100% strain; a self-assembled monolayer ensures robust interlayer adhesion in strained, aqueous conditions; a complementary p–n organic electrochemical transistor architecture that counterbalances strain-induced current variations. The resulting amplifiers maintain high gain under >50% deformation and directly capture and amplify in vivo biosignals with substantially improved signal-to-noise ratios, establishing a route to mechanically resilient, high-fidelity bioelectronic interfaces.

In vivo biosignal acquisition is critically important because it enables continuous monitoring of physiological states and supports fundamental biological research with real-time clinical diagnostics[1,2]. The accurate decoding of biological activity relies on efficiently acquiring high-quality biosignals with minimal distortion under dynamic biological environments (Fig. 1a). To achieve this, an ideal in vivo biosensor should establish a seamless tissue/machine interface and in situ signal amplification capability, as weak biosignals are easily attenuated or contaminated by noise at the biotic/abiotic interface. However, the development of such biosensors faces several challenges: (1) The dynamic movement of organs and tissues during daily activities[3] leads to the intrinsic failure of devices in this aqueous environment, such as corrosion, delamination and dissolution[4]. (2) Weak biosignals are highly susceptible to noise coupling through the biotic/abiotic interface and wires of the sensor. (3) Inflammatory reactions or the formation of scar tissue due to a mechanical mismatch and poor biocompatibility can

[1]State Key Laboratory of Advanced Waterproof Materials, Engineering Research Center of Ministry of Education for Adaptive Biomaterials and Medical Devices, School of Materials Science and Engineering, Peking University, Beijing, China. [2]School of Mechanical Engineering, Dalian University of Technology, Dalian, China. [3]Department of Orthopaedics, Peking University Third Hospital, Beijing, China. [4]Beijing Key Laboratory of Advanced Bioadaptable Orthopedic Implants, Beijing, China. [5]Engineering Research Center of Bone and Joint Precision Medicine, Ministry of Education, Beijing, China. [6]Department of Spinal Surgery, Peking University People's Hospital, Beijing, China. [7]Beijing National Laboratory for Molecular Sciences (BNLMS), Key Laboratory of Polymer Chemistry and Physics of Ministry of Education, Center of Soft Matter Science and Engineering, College of Chemistry and Molecular Engineering, Peking University, Beijing, China. [8]School of Microelectronics, University of Science and Technology of China, Hefei, China. ✉e-mail: zhizhang@pku.edu.cn; tinglei@pku.edu.cn

https://doi.org/10.1038/s44460-026-00091-7

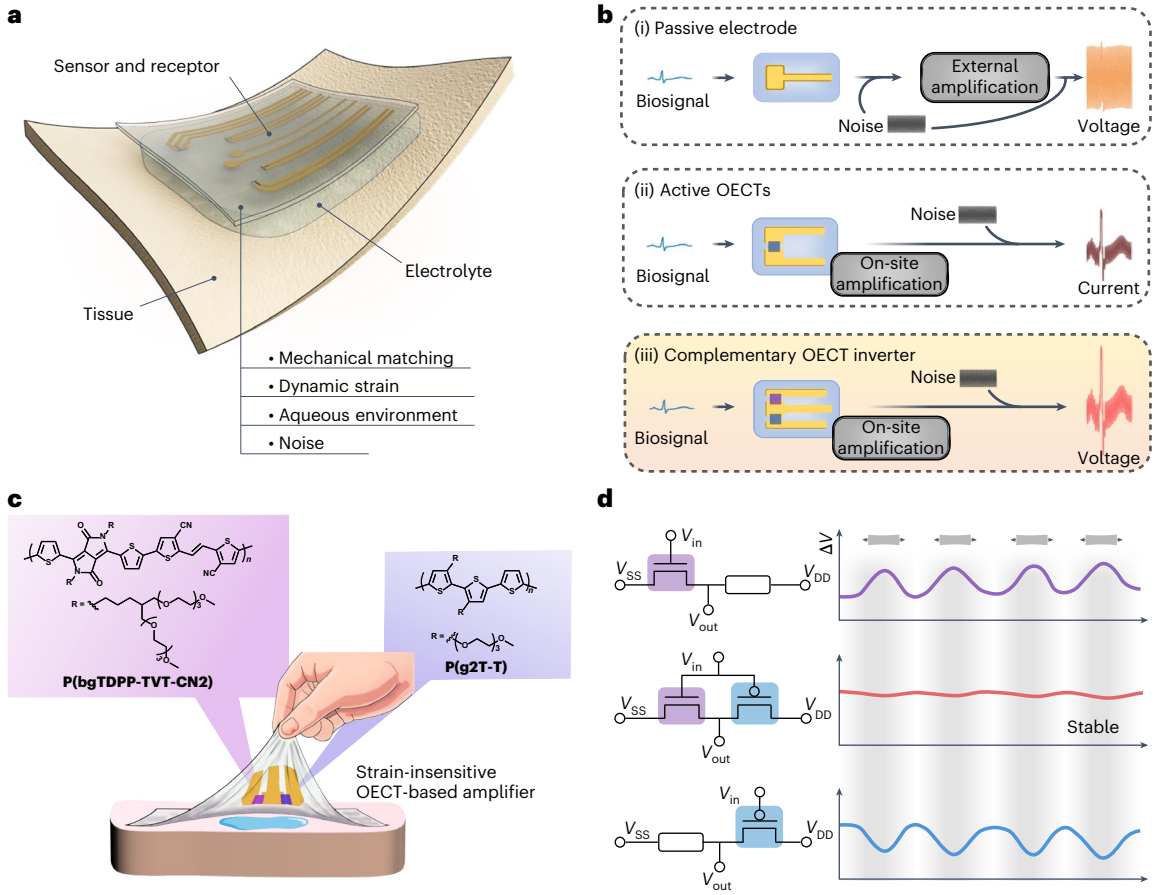

Fig. 1 | Strain-insensitive amplifier design and its application in bioelectronics. **a**, Schematic diagram of sensors or receptors for in vivo electrophysiological recording. **b**, Advantage of in vivo amplification by active OECT amplifiers, compared with passive electrodes and single-transistor devices. **c**, Schematic diagram of the elastic electrophysiological amplifier based on an OECT inverter. **d**, Designs of paired OECT circuits for strain-insensitive operation through current compensation. V_{in}/V_{out}, input/output voltage; V_{DD}/V_{SS}, positive/negative supply voltage; ΔV, deviation in V_{out}.

change the interface environment and jeopardize long-term recording stability[5]. Consequently, it is essential to develop soft, stretchable—or even elastic—biosensors with an in vivo amplifying capability to allow stable signal-recording.

Soft and stretchable electrodes are used for in vivo applications due to their good biocompatibility and seamless tissue integration[6–9]. However, their performance is often limited by low signal-to-noise ratios (SNRs) caused by high interfacial impedance and noise from wiring and back-end electronics, which restricts their effectiveness in making high-fidelity recordings[10,11]. Intrinsically stretchable or elastic organic field-effect transistors have been extensively used for complex logic circuits in signal processing[12–14]. However, they cannot work directly in an aqueous environment. Thus, complex packaging is required, which often compromises softness and stretchability, and their high operating voltage (often >10 V) may pose safety concerns for tissue[14]. Organic electrochemical transistors (OECTs) have emerged as promising candidates for simultaneous in vivo biosignal acquisition and amplification due to their distinct advantages, such as low operating voltage (<1.0 V), operability in aqueous environments and high biocompatibility[15,16]. Although soft single-OECT devices have been successfully employed to record and amplify biosignals (Fig. 1b)[17–21], they still face two main challenges: (1) Their current output is not directly compatible with commercial electrophysiological acquisition systems[22,23] and (2) their strain sensitivity can induce current drifts, which substantially compromise the stability and reliability of signal-recording.

Unlike single-OECT devices, amplifiers based on complementary OECT inverter circuits can simultaneously record and amplify biosignals in situ and produce a voltage output, which facilitates their integration with back-end acquisition systems[23,24], and do so with an enhanced SNR[3,25] (Fig. 1b). To construct a complementary amplifier, both p-type and n-type OECTs are necessary. However, to date, only a few p-type OECT materials with intrinsic stretchability have been reported[19,26–29], and stable and intrinsically stretchable n-type materials remain unavailable, leaving a gap in the development of stretchable and elastic in vivo amplifiers. Additionally, effective strategies for minimizing strain-induced current drifts in practical OECT devices have not yet been explored, further limiting their reliability under physiological motion.

Here we demonstrate an integrated strain-insensitive material, device and circuit design, which we used to build an elastic, biocompatible and stable in vivo amplifier for biosignal-recording (Fig. 1c). First, we developed an n-type OECT material, P(bgTDPP-TVT-CN2), with high electrical performance and stretchability, which retains its transconductance (g_m) with only minimal variation, even under 100% strain. Second, by pairing this material with a p-type counterpart, we constructed stretchable complementary OECT inverters exhibiting a high voltage gain of 140 V/V. Importantly, the complementary OECT configuration compensates for strain-induced current variations, thereby eliminating drift and enhancing strain stability in practical applications (Fig. 1d). Third, a self-assembled monolayer (SAM) was employed to improve device stability during repeated deformation in aqueous environments, thus enabling stable in vivo operation. Finally, having validated its biostability and biocompatibility, we applied the fully elastic OECT amplifier to record in vivo

https://doi.org/10.1038/s44460-026-00091-7

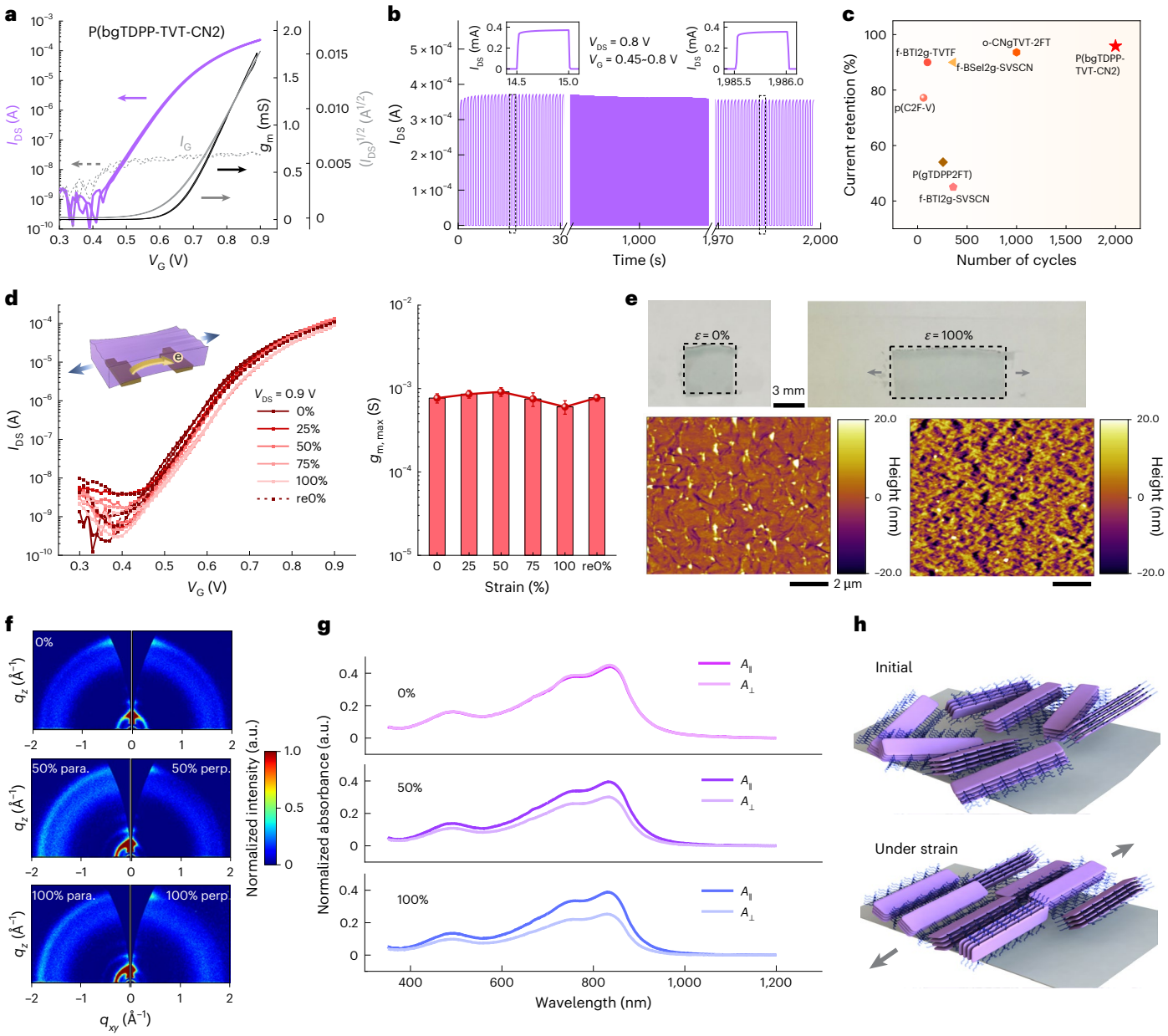

Fig. 2 | Electrical performance and morphology characterization of P(bgTDPP-TVT-CN2) with different strain levels. a, Transfer characteristics of a P(bgTDPP-TVT-CN2)-based OECT device. The dashed curve represents the gate current (I_G). **b**, Operational stability of a P(bgTDPP-TVT-CN2) OECT device over 2,000 on/off cycles (V_G = 0.45–0.8 V, pulse width = 0.5 s and V_{DS} = 0.8 V). Insets: single pulses at the beginning and end of the test. I_{DS}, drain-source current; V_{DS}, drain-source voltage; V_G, gate voltage. **c**, Comparison of the stability during cycling of P(bgTDPP-TVT-CN2) OECT with other reported n-type OECTs[39] whose μC^* is higher than 50 F cm^{-1} V^{-1} s^{-1}. **d**, Transfer characteristics and maximum transconductance g_m of P(bgTDPP-TVT-CN2) under different strain levels. re0%, recovered to 0% strain. Inset: schematic of an OECT device with strained channel material. Data are presented as mean values ± standard deviation (n = 10 for 0% strain and n = 5 for other strain levels, where n is the number of OECT devices). **e**, Photographs (top) and AFM height images (bottom) of P(bgTDPP-TVT-CN2) films under 0% and 100% strain ε. **f**, GIWAXS results for P(bgTDPP-TVT-CN2) films under 0%, 50% or 100% strain. Para., parallel; perp., perpendicular. **g**, Polarized UV-vis-NIR spectra of P(bgTDPP-TVT-CN2) films under different strain levels. **h**, Schematics showing the rotation and alignment of the polymer crystalline structure under strain.

electrocardiogram (ECG) signals, thus demonstrating its conformal and stable attachment on wet heart tissues as well as its superior SNR and drift-free advantages.

Highly stretchable and stable n-type material

When designing the stretchable n-type material, we first selected thiophene-flanked diketopyrrolopyrrole (TDPP) as the core building block due to its highly planar backbone and high charge carrier mobility[30]. Reducing the crystallinity and glass transition temperatures of conjugated polymers is an effective approach for realizing high stretchability. Thienylenevinylenethiophene (TVT) has been shown to reduce polymer crystallinity while maintaining a high charge mobility[31]. However, TVT is an electron-donating building block, making it unsuitable for n-type OECTs[32]. To address this, cyano (CN) groups were added to the TVT to stabilize negative polarons and enhance the uniformity of the negative charge distribution[32,33] (Supplementary Fig. 2). Additionally, grafting branched ethylene glycol side chains onto the TDPP backbone facilitated good solubility and ion transport within the polymer bulk[34] while simultaneously reducing the crystallinity to improve the overall stretchability[35,36].

The performance of the resulting polymer, P(bgTDPP-TVT-CN2), as an OECT was evaluated using a photolithography and double-layer parylene patterning method[37]. The polymer exhibited typical n-type OECT behaviour, with a figure-of-merit value μC^* (ref. 38) of 163.3 ± 5.8 F cm^{-1} V^{-1} s^{-1}(Fig. 2a and Supplementary Fig. 1). More importantly, the polymer exhibited exceptional operational stability among n-type OECTs with μC^* beyond 50 F cm^{-1} V^{-1} s^{-1} (ref. 39; Supplementary Table 1). The polymer maintained 95.9% of its initial performance after 2,000 switching cycles, and 81.1% after 30,000 switching cycles (Fig. 2b,c and Supplementary Figs. 3 and 4). Repeated cyclic voltammetry curves confirmed its electrochemical stability (Supplementary Fig. 5), which indicates its potential for practical applications. Furthermore, P(bgTDPP-TVT-CN2) demonstrated notable stretchability. The OECT performance was evaluated under strain levels of 0% to 100% using a transfer method, as previously reported[19]. When stretched parallel or vertical to the charge-transfer direction and then allowed to recover, the OECT performance of P(bgTDPP-TVT-CN2) remained stable with limited variations of the transconductance. Both the maximum transconductance $g_{m,max}$ (defined as $(\partial I_D/\partial V_G)_{max}$) and μC^* exhibited minimal fluctuations under different strain levels in both directions, indicating that the electrical performance of the polymer was largely insensitive to mechanical deformation (Fig. 2d and Supplementary Figs. 6 and 7).

To investigate the mechanism underlying the high stretchability, we calculated the dihedral angle and torsional barrier using density functional theory. The results revealed that the torsion angle between the TDPP and TVT segments was ~30°, and the torsional barrier was lower than that of other rigid conjugated polymers[40], leading to a twisted backbone curvature (Supplementary Fig. 8). We propose that this twisted backbone reduces the polymer crystallinity and enhances the interchain entanglement, thereby improving stretchability.

A grazing-incidence wide-angle X-ray scattering (GIWAXS) analysis of the unstretched film found a relatively amorphous molecular packing with a mixed face-on and edge-on orientation (Fig. 2f). Upon stretching to 50% and 100% strain, the diffraction intensity became anisotropic, as it differed for when the X-ray beam was parallel to the strain direction compared with when it was perpendicular to the strain direction. When the X-ray beam was parallel to the strain direction, the π−π stacking diffraction in the in-plane (q_{xy}) direction was enhanced, while the diffraction in the out-of-plane (q_z) direction decreased; the opposite trend was observed during perpendicular incidence (Fig. 2f and Supplementary Fig. 9). This result indicates the polymer packing underwent rotation and reorientation during stretching (Fig. 2h). Polarized ultraviolet–visible–near-infrared (UV-vis-NIR) spectroscopy revealed that when the polymer was stretched from 0% to 100%, the difference between the absorption intensity with the polarization parallel ($A_{\parallel}$) and the absorption intensity with the polarization perpendicular ($A_{\perp}$) to the stretching direction increased. The dichroic ratio, defined as the ratio of $A_{\parallel}$ and $A_{\perp}$ (ref. 41), continuously increased, indicating that the polymer chains became aligned during stretching (Fig. 2g and Supplementary Fig. 10). This alignment and rearrangement of the polymer chains may account for the slight increase in the maximum g_m as the strain was increased. These results demonstrate that the reorientation-induced stress dissipation of the initially amorphous and entangled chains contribute to the high intrinsic stretchability of P(bgTDPP-TVT-CN2). Moreover, we hypothesize that its outstanding operational stability may also stem from its low crystallinity, as amorphous films are less sensitive to morphology changes induced by ion injection and ejection (Supplementary Fig. 11).

Furthermore, optical microscopy and atomic force microscopy (AFM) height images of films transferred onto a polydimethylsiloxane (PDMS) substrate and stretched to 100% strain reveal that the films remained intact without marked large cracks (Fig. 2e). To evaluate its stability under repeated cycles of stretching, the polymer film was subjected to cycles with 30% strain, which exceeds the typical strain levels encountered in physiological tissue, such as the heart (15–20%)[3]. After 1,000 cycles of stretching, $g_{m,max}$ showed no substantial decline, further demonstrating the excellent cyclic stretching stability of the polymer. Further high-strain cycling tests also supported its outstanding stretchability (Supplementary Fig. 12). This stretchable and stable n-type material provides a reliable material basis for the construction of elastic OECT amplifiers.

Elastic OECT fabrication and strain-insensitive circuit

To translate the above material advances into OECT amplifiers, we designed an elastic OECT circuit for reliable sensing under dynamic deformation. We first built an elastic n-type OECT device using a lamination method. It consisted of an active layer (P(bgTDPP-TVT-CN2)), an elastic substrate (styrene-ethylene-butylene-styrene, SEBS), a pre-stretched Au electrode and an encapsulation layer (PDMS) (Fig. 3a).

During repeated stretching in aqueous environments, however, we observed progressive delamination of the polymer, particularly near the crack edges that formed in the Au electrode, which caused pronounced performance fluctuations (Supplementary Fig. 13). To enhance operational stability, we added a benzyl mercaptan SAM onto the Au surface via vapour-phase modification. This interfacial SAM effectively improved underwater adhesion and operational stability through two primary mechanisms (Fig. 3b): (1) π−π interactions between the SAM and the conjugated polymer backbone and (2) an increase in the surface energy of the Au, as evidenced by an increase in the contact angle from 36.9° to 67.6°, which promoted adhesion between the hydrophobic polymer backbone and the Au surface (Supplementary Fig. 13c). In addition, the SAM facilitated the transfer process, which boosted the fabrication yield while exerting negligible influence on the electrical performance (Supplementary Fig. 13d). The successful fabrication of a high-performance p-type stretchable OECT based on P(g2T-T)[19] (Supplementary Fig. 14) validated the effectiveness and universality of this process.

Benefiting from the pre-strained Au electrode and SAM modification, both the p- and n-type OECT devices exhibited good semiconducting properties as the strain was increased (Fig. 3c), although their on-current slightly decreased due to inevitable changes in the channel dimensions. Most studies to date have primarily focused on maintaining the normalized transconductance ($g_{m,n}$) under strain while overlooking current variations. In practical applications, however, strain-induced dimension variations directly affect the output current, leading to pronounced strain sensitivity. Consequently, circuits based on a single stretchable transistor, such as load-diode inverters, cannot sustain a stable output under mechanical strain[42,43] (Supplementary Fig. 16 and Supplementary Note 2), which restricts their applications primarily to strain or tactile sensors[44]. This strain sensitivity poses a major challenge for the practical application of biosensors, particularly those making electrophysiological recordings, as fluctuations induced by tissue motion can compromise signal accuracy. Therefore, realizing strain-insensitive biosensors remains a challenge for stretchable and elastic electronics.

To overcome this limitation, we propose a complementary design for an inverter circuit. This design leverages the synchronous changes in the current of both p-type and n-type OECTs during stretching. These changes effectively counterbalance each other and act as a self-reference, thereby rendering the circuit less susceptible to strain.

To validate this concept, we first fabricated a complementary inverter circuit on a rigid substrate by integrating P(g2T-T) with our stretchable n-type polymer, P(bgTDPP-TVT-CN2), using the aforementioned transfer method. Each of the two types of polymer film was picked up by a PDMS film, stretched and then transferred onto the same rigid substrate, where they were connected using gold wires (Supplementary Fig. 17). For comparison, a load-diode inverter circuit made from a constant resistor and a P(bgTDPP-TVT-CN2)-based OECT

https://doi.org/10.1038/s44460-026-00091-7

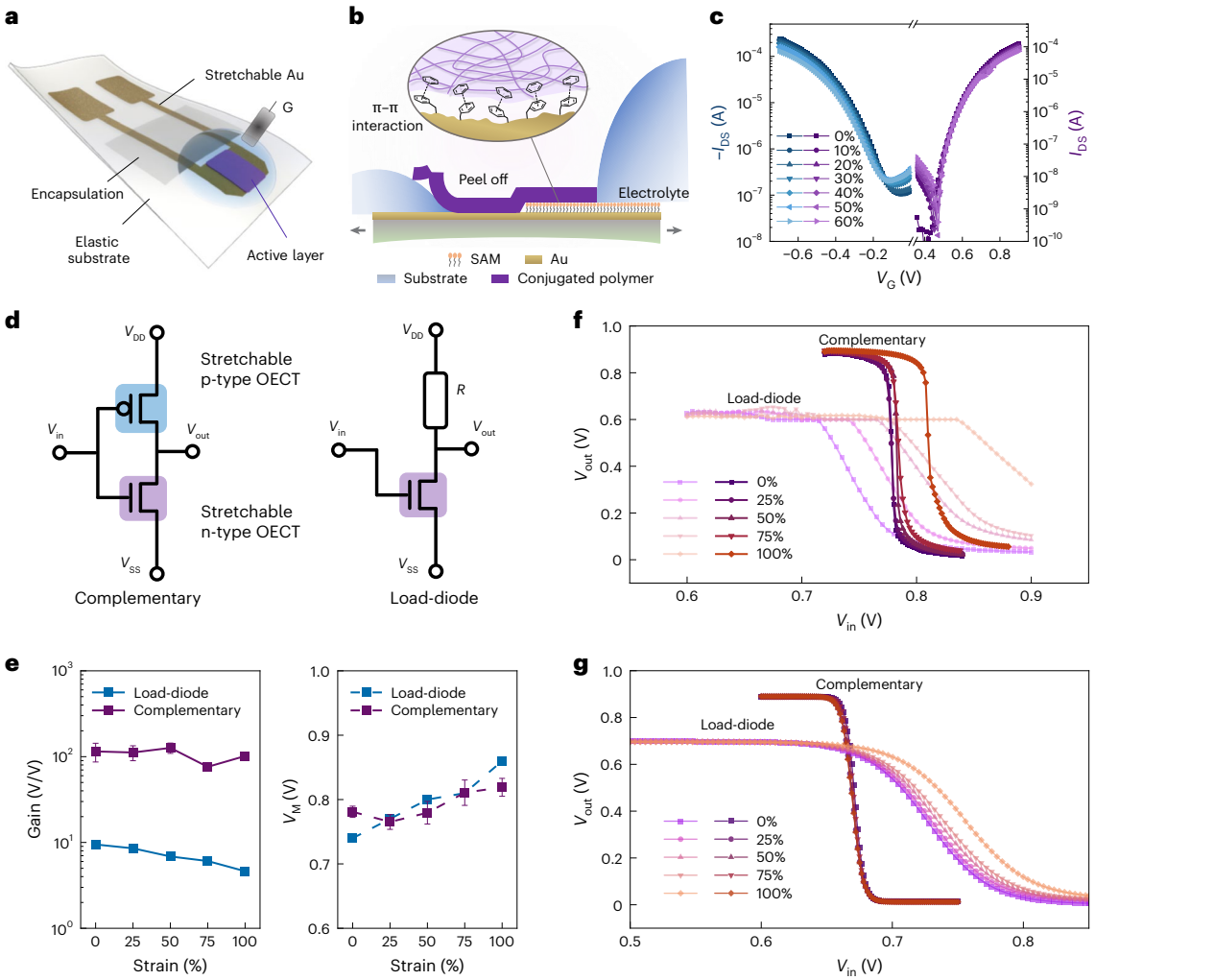

Fig. 3 | Fabrication of an elastic OECT device and strain-insensitive circuit design. a, Schematic illustration of an elastic OECT device. G the gate electrode. **b**, Schematic diagram of the function of the benzyl mercaptan SAM modification. **c**, Transfer curves of elastic n- and p-type OECTs under different strain levels (W/L = 400 µm/40 µm). The electrolyte was 0.1 M NaCl solution, and the gate was an Ag/AgCl electrode. **d**, Schematic diagrams of the complementary circuit and the load-diode circuit. **e**, Gain and V_M for each device (rigid substrate, W/L = 100 µm/10 µm) in **d** under different strain levels. Data are presented as mean values ± standard deviation (n = 10 for 0% strain and n = 5 for other strain levels, where n is the number of inverter devices). **f**,**g**, VTCs for the two devices in **d** under different strain levels based on experimental data (V_{DD} = 0.9 V and V_{SS} = 0 V) (**f**) and simulation results (**g**). The data at 100% strain in **f** showed moderate changes, mainly due to the unmatched stretchability of the n-type and p-type materials.

was used as a reference (Fig. 3d). The voltage transfer characteristic (VTC) curves of the load-diode circuit shifted notably as the device was stretched from 0% to 100%, mainly due to the decrease of the strain-induced current for a single OECT (Fig. 3e,f). As a result, the maximum gain (defined as dV_{out}/dV_{in}) decreased from 9.47 V/V to 4.62 V/V, and the switching threshold voltage (V_M, the corresponding V_{in} voltage when V_{out} potential is $(V_{DD} + V_{SS})/2$) consistently increased from 0.74 V to 0.86 V. Such a large voltage shift will induce large artefacts, making it unsuitable for practical biosensing. By contrast, the VTC of the complementary circuit showed minimal changes, with a slight V_M shift from 0.781 V to 0.811 V (+3.8%) under strain levels of up to 75%. The gain value of the complementary circuit remained consistently high, around 80 V/V, thus ensuring stable operation and analogue signal amplification. We also evaluated the output of the two circuits under assumed dynamic deformations by applying a 25% cyclic tensile strain, yielding time-dependent output curves (Supplementary Fig. 19). The simulated results showed that the load-diode circuit exhibited more notable output fluctuations under cyclic strain, whereas the output of the complementary circuit remained relatively stable, which demonstrates the strain insensitivity of this circuit design.

We supported the current counterbalance mechanism using a load-line simulation method. Assuming that the performance of the p-type and n-type OECTs decreases synchronously with increasing strain, the output curves of both devices were superimposed to obtain VTC curves (Supplementary Figs. 20–23 and Supplementary Note 3). The simulation results demonstrate that the complementary design exhibits superior output stability upon stretching, which agrees well with the experimentally measured trend (Fig. 3g). Given these results, our complementary design substantially mitigates the strain-sensitive nature of individual transistors, thus enabling more complex and reliable sensing applications.

Fabrication and performance of the elastic, aqueous-stable amplifier

The above inverter was then used as an elastic small-analogue-signal amplifier for in vivo applications (Fig. 4a). The fabrication process is illustrated in Supplementary Figs. 24 and 25. Given that the p-type and n-type OECTs did not have a well-matched threshold voltage V_{th} or on-state current (Fig. 3c), we first systematically adjusted the width-to-length (W/L) ratio of the p-type OECT to reduce its on-state current

https://doi.org/10.1038/s44460-026-00091-7

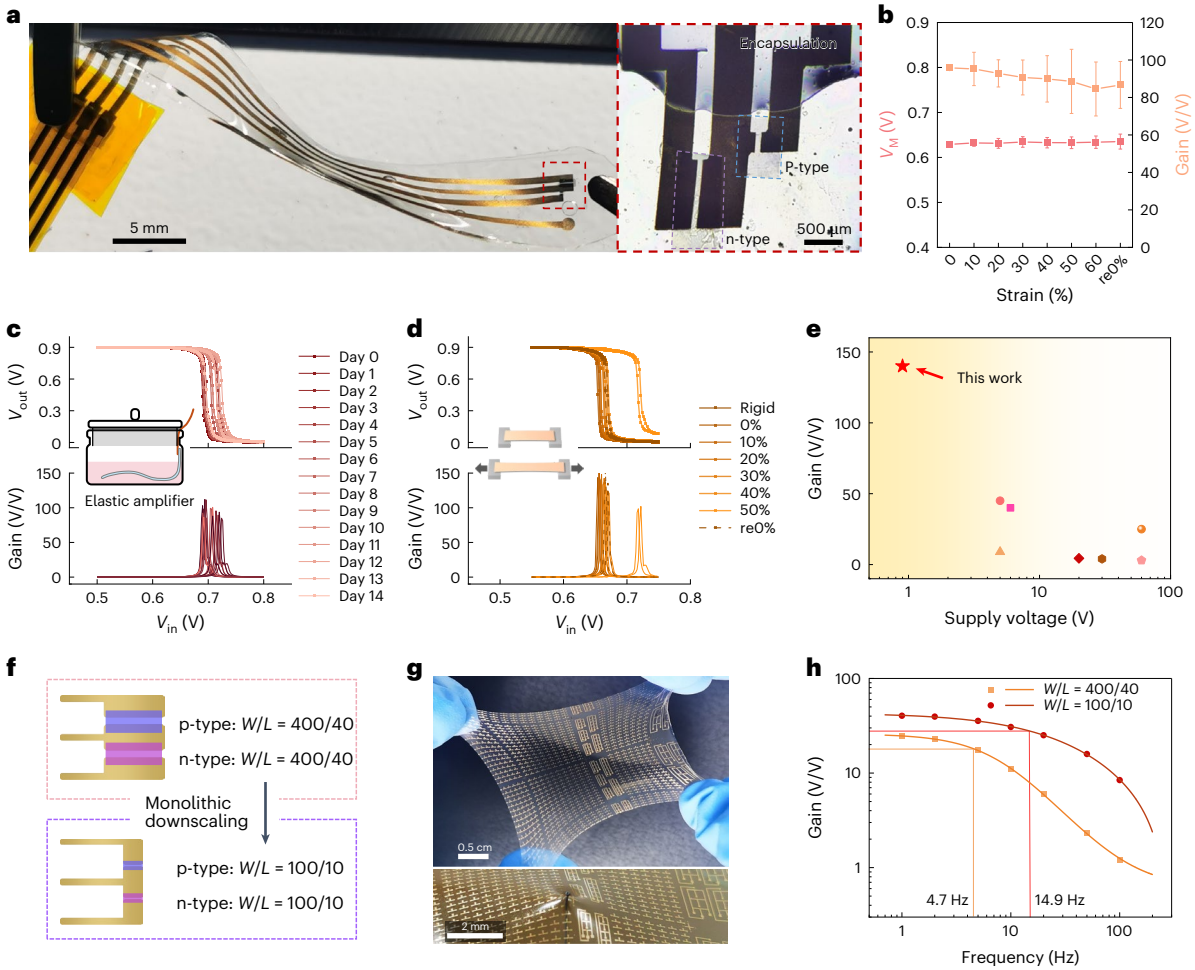

Fig. 4 | Characterization of the elastic amplifier for in vivo application. **a**, Photograph of the elastic amplifier for in vivo applications. Inset: magnified image of the channel region of the device. **b**, Normalized gain and V_M of the elastic amplifier under different strain levels from the VTC. Data are presented as mean values ± standard deviation (for eight different elastic amplifiers). **c**, Summary of daily VTC curves and gain values for the elastic amplifier in a blood plasma environment. Inset: the experimental set-up. **d**, Summary of VTC curves and gain values for the elastic amplifier under different strain levels. **e**, Comparison of the gain value and supply voltage of different stretchable inverters[13,14,45–47,49,50]. **f**, Schematic diagram of the monolithic downscaling of the channel area of the amplifier. **g**, Photographs of the miniaturized elastic amplifier. **h**, Dynamic responses of the elastic amplifier before and after channel area downscaling. The input signal was a 20-mV sinusoidal signal at different frequencies with a d.c. bias at V_M.

(Supplementary Fig. 27a). After optimization, the transfer characteristics of the two materials aligned much better, resulting in a reduction of V_M from 0.8 V to 0.65 V (Supplementary Fig. 27b,c). Lowering V_M not only minimizes power consumption and the bias potential required for signal amplification but also reduces the risk of potential tissue damage.

Benefiting from the good operational stability and the inherent current counterbalancing of our complementary design, the amplifier output remained notably stable. Both the gain value and V_M exhibited minimal variation across different strain levels (Fig. 4b and Supplementary Figs. 29–31). Notably, the SAM-modified amplifier remained fully functional even after 14 days of immersion in rabbit plasma and 24 days in phosphate-buffered saline (PBS) solution (Fig. 4c and Supplementary Figs. 32 and 33). This finding underscores the outstanding operational stability of our n-type polymer in physiological environments.

To ensure suitability with in vivo implantation, the elastic amplifier was designed as a long strip (Supplementary Fig. 36a). A bonded anisotropic conducting film and flexible printed circuits (FPCs) were used for the electrical connections. Having been designed for electrophysiological recording, the amplifier showed a maximum gain of about 140 V/V with a negligible variation in V_M and gain under 0% to 40% strain (Fig. 4d and Supplementary Fig. 36b). Both the operational voltage and gain of the elastic amplifier are exceptional among reported stretchable inverters made from organic or inorganic materials[13,14,45–47] (Fig. 4e and Supplementary Table 3). A simulated electroencephalogram signal was amplified about 40 times (Supplementary Fig. 36c). Under bended and tented deformation, the elastic amplifier also demonstrated good amplification (Supplementary Figs. 37 and 38). Moreover, the amplification capability remained unaffected under dynamic strain levels (Supplementary Figs. 39 and 40 and Supplementary Note 6). These results show that the elastic amplifier is fully suitable for most electrophysiological recording applications, as large-deformation tissues, such as the skin or heart, typically experience a strain of no more than 30% during daily activities[3].

To investigate the dynamic response, we simulated weak electrophysiological signals by applying a 20-mV sinusoidal signal input with a d.c. bias to V_M. The resulting ~25-fold amplification at 1 Hz was lower than the gain obtained from the VTC curve (Fig. 4h and Supplementary Fig. 42). This limited performance stemmed from the oversized channel and the high electrode capacitance (Supplementary Fig. 43). To address this, we devised a monolithic photolithography fabrication process to downscale the channel size (Fig. 4f and Supplementary Fig. 44), which demonstrates the integration potential of the elastic amplifier. Miniaturizing the channel to 10 μm notably enhanced the dynamic response (Fig. 4g and Supplementary Fig. 45). It achieved a 40-fold magnification at 1 Hz and a 14.9-Hz cutoff frequency under a 20-mV sinusoidal input (Fig. 4h). Furthermore,

https://doi.org/10.1038/s44460-026-00091-7

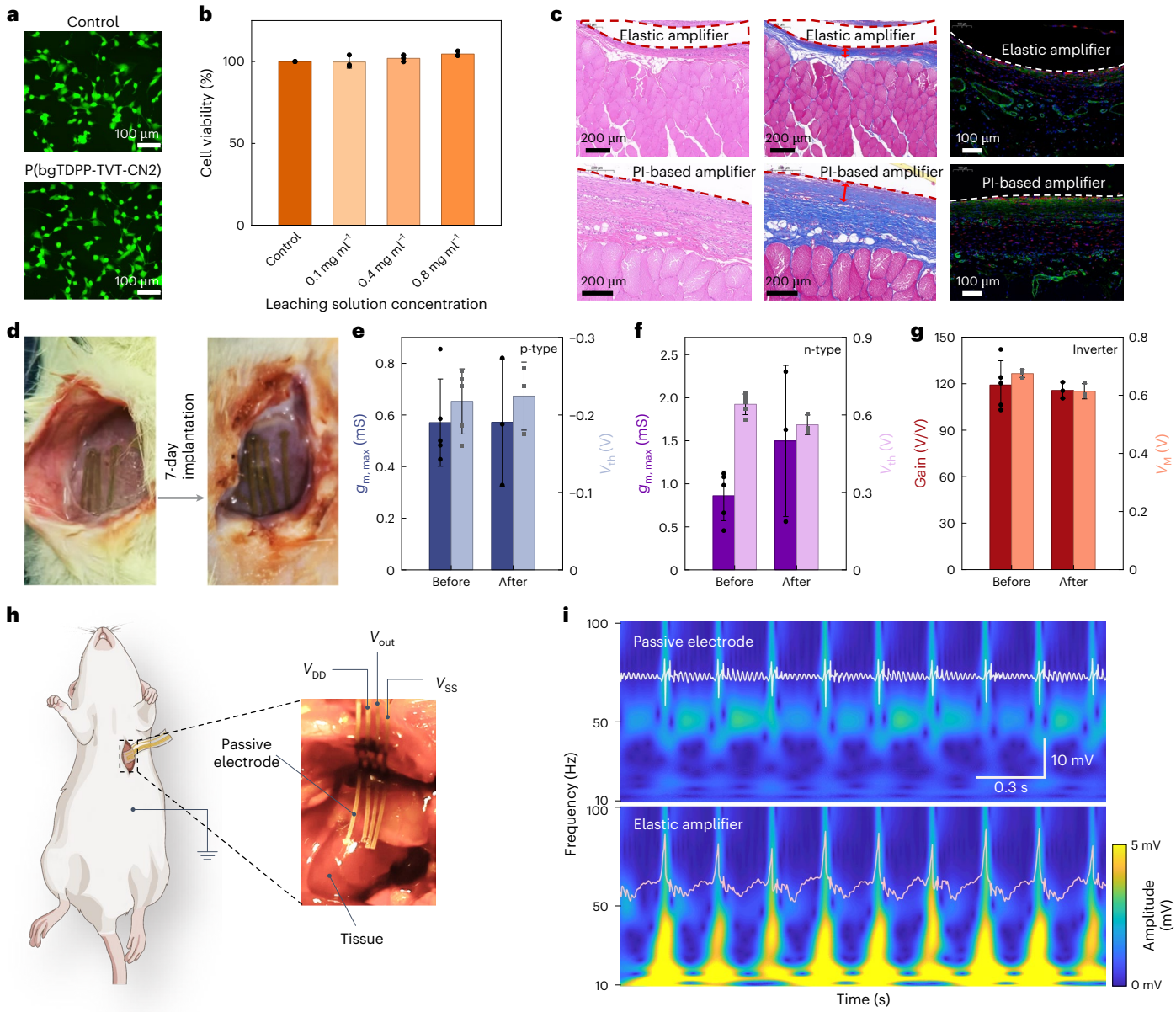

Fig. 5 | Elastic amplifiers for implantable bioelectronics. a, Cell staining images of the polymer film and a control sample in a live/dead staining test. **b**, Cell viability of mouse fibroblasts (NIH-3T3) from the MTT assay. Data are presented as mean values ± standard deviation (over three independent experiments). **c**, Comparison of histological results for an elastic (thickness ~400 µm) and PI-based (thickness ~25 µm) amplifier. Representative images with haematoxylin and eosin, Masson's trichrome and immunofluorescence staining are shown from left to right. **d**, Photographs of the device before and after implantation for 7 days. **e**–**g**, Performance statistics of the device before and after implantation: g_m and V_{th} of p- (**e**) and n-type (**f**) OECTs and the gain of the amplifier and V_M (**g**). Data are presented as mean values ± standard deviation ($n = 5$ for the data before implantation and $n = 3$ for the data after implantation, where n is the number of inverter devices implanted in different rats). **h**, Schematic of the electrical set-up and a photograph of a device used for in vivo ECG. **i**, Time-domain ECG signals obtained by the elastic amplifier and its time–frequency analysis diagram, compared with those for a passive electrode.

although the mesoscale amplifier magnified a simulated ECG signal by only six times, the microscale amplifier achieved over 25-fold magnification (Supplementary Fig. 46 and Supplementary Note 7). However, at a 10-µm resolution, the stretchability of the microscale device is constrained by the Au electrodes to no more than 30% strain. As optimizing the stretchability of the micro-cracked Au is beyond the current scope, only the mesoscale device was used for the subsequent in vivo scenario.

Enhanced biocompatibility and in vivo electrophysiological recording

Biocompatibility, biostability and stable electrical performance are essential for implantable biosensors. We first evaluated the biocompatibility of the polymer with cell viability tests using mouse fibroblasts (NIH-3T3), and the semiconducting polymer P(bgTDPP-TVT-CN2) showed low cytotoxicity (Fig. 5a,b). Next, we conducted a long-term in vivo histological comparison against conventional polyimide (PI)-based devices (Supplementary Fig. 48). After 6 weeks of subcutaneous implantation, our elastic amplifier formed a stable, mature fibrous capsule. There was a thin, compact collagen layer with minimal inflammatory cell infiltration (mature collagen fraction 8.5%). By contrast, the PI-based flexible device showed continuing tissue remodelling and chronic inflammation, characterized by a thicker collagen layer, abundant capillaries and scattered nuclei (mature collagen fraction 15.5%). Overall, this compact capsule demonstrates the better

tissue integration and higher biocompatibility of this elastic amplifier compared with its PI counterparts (Fig. 5c and Supplementary Fig. 49).

To further investigate the in vivo stability, elastic amplifiers were subcutaneously implanted in the rat hindlimb for 1 week (Fig. 5d). Post-implantation tests showed that both p-type and n-type OECT materials maintained their semiconducting properties (Fig. 5e,f and Supplementary Fig. 50a). The p-type OECT maintained its g_m but had a lower on/off ratio and increased V_{th} (probably from reductive doping). By contrast, the n-type OECT exhibited improved performance (enhanced g_m and reduced V_{th}) after implantation, possibly due to further doping by endogenous reducing chemicals, such as dopamine, ascorbic acid, catalase and so on. Interestingly, such performance variations helped to compensate for the inherently high V_{th} of the n-type material, such that the performances of the n-type and p-type OECTs better matched. Overall, the amplifier maintained a stable gain of 120 V/V after 7 days of implantation. It then had a smaller V_M closer to 1/2 of V_{DD}, which would allowing operation at a lower voltage (Fig. 5g and Supplementary Fig. 50b). These results demonstrate the robust in vivo adaptability of our elastic amplifier and its reliable signal amplification.

Following the biocompatibility and biostability assessment, we performed in vivo recording and amplification of the ECG signal in a Sprague Dawley rat (Fig. 5h). The PI-based flexible amplifier showed poor adhesion to the beating heart surface due to its high modulus, and its output was uninterpretable. By contrast, our elastic device, with its low modulus and low stiffness (Supplementary Figs. 47 and 48), maintained seamless adherence during vigorous motion. A planar Au electrode was fabricated alongside the elastic amplifier to enable simultaneous recording. As shown in Fig. 5i, ECG signals with a rhythm of 270 beats per minute were recorded by both the passive electrode and the elastic amplifier. During the test, the motion of the tissue was also captured and magnified by the device, as evidenced by the low-frequency fluctuations in the trace. Because of the high-frequency range of the rat ECG signals, the amplification factor was limited to three times. Nevertheless, the amplifier achieved a notably higher SNR of 25.12 ± 3.20 dB compared with the passive electrode (11.08 ± 2.62 dB), as the in situ amplification mainly suppressed external wiring noise. Additionally, we successfully recorded the lower-frequency ECG signal of a rabbit using the elastic amplifier, achieving over 10 times magnification (Supplementary Fig. 51). Further device optimization, including reducing the channel length or adopting new device configurations[14,48], could substantially enhance the dynamic response of the amplifier, leading to improved magnification and SNR for a broader range of electrophysiological applications.

Conclusions

In summary, we have demonstrated an elastic in vivo amplifier that can work intimately in wet, dynamic biological environments. This advance was enabled by three key innovations: (1) the development of a highly stretchable and high-performance n-type polymer, P(bgTDPP-TVT-CN2), (2) a hydrophobic SAM that enhances adhesion for conjugated polymers and (3) a complementary circuit design that effectively mitigates strain sensitivity. With these innovations, we fabricated elastic amplifiers capable of achieving high voltage gains of up to 140 V/V while operating at low voltages (<1.0 V) in aqueous environments. The devices were successfully applied in vivo to record ECG signals, and they demonstrated conformal and stable attachment to wet heart tissue while delivering superior SNR. Although further optimization is needed to improve response times and amplification factors, this work establishes a viable pathway for achieving stable, long-term, in vivo recording and amplification of biosignals, even under large deformations and in dynamic biological environments.

Methods

Synthesis of OECT materials

The synthesis procedures for P(bgTDPP-TVT-CN2) and P(g2T-T) are detailed in Supplementary Note 1.

General materials characterization and calculation

Polarized UV-vis-NIR spectra were recorded on a UV-vis-NIR spectrophotometer (UV3600-Plus, Shimadzu) equipped with a polarizer to control the polarization direction relative to the stretching direction. Cyclic voltammetry tests were performed with an electrochemical workstation (SP-300, BioLogic Science Instruments) in 0.1 M tetrabutylammonium hexafluorophosphate (n-Bu_4NPF_6)/acetonitrile solution with ferrocene/ferrocenium (Fc/Fc^+) as the external standard. AFM topography measurements were performed with an atomic force microscope (Cypher, Asylum Research, Oxford Instruments). Surface morphology was recorded at a scan rate of 1–2 Hz in a.c. mode. The AFM modulus was measured with an atomic force microscope (MultiMode 8, Bruker), and Young's modulus was extracted using the DMT contact mechanics model. All data were processed and analysed using Nanoscope Analysis software (Bruker). Two-dimensional GIWAXS measurements were conducted on a XenocsSAXS/WAXS system with an X-ray wavelength of 1.5418 Å and an incidence angle of 0.2°. Pilatus 300K was used as a two-dimensional detector. Data processing was performed using Nika and WAXTools packages in Igor Pro.

Geometry optimization and relaxed potential energy surface scans were performed at the ωB97XD/6-311 g(d,p) level using Gaussian 16 and Gauss View 6.

Fabrication and characterization of rigid OECT devices

The OECT devices were fabricated following the reported double-parylene method with minor modifications[37]. First, the silica substrate was ultrasonically washed in acetone, deionized water (DI) water and isopropyl alcohol in sequence, followed by drying with nitrogen and oxygen plasma for 5 min (PDC-MG, Chengdu Mingheng). Source and drain electrodes were fabricated by a lift-off method, which included photo-patterning a photoresist LOR 3A/S1813 using a UV lithography machine (MA6, SUSS), magnetron sputtering of 5 nm Ti and 40 nm Au (QAM-4W-STS, ULVAC), and removing the patterned photoresist and excess metal. Subsequently, a 1-μm layer of parylene-C was chemically deposited using a PDS 2010 Labcoater-2 (Specialty Coating Systems), after applying 3-(trimethoxysilyl)propyl methacrylate (A-174 silane), which is an adhesion promoter, onto the substrate. An anti-adhesive layer (2 v/v% Micro-90 water solution) was subsequently spin-coated onto the first layer at 1,000 rpm for 1 min, followed by the deposition of another 1-μm layer of parylene. An AZ 10XT photoresist and AZ-400K developer were then used to expose the channel while protecting the other parts. The exposed channel areas were etched by reactive-ion etching with O_2 plasma using a reactive-ion etcher (LCCP-6A, Leuven Instruments). Finally, the excess photoresist was rinsed off with acetone.

A P(bgTDPP-TVT-CN2)/chloroform solution (3 mg ml^{-1}) was spin-coated onto the devices in a glovebox to form a 30–60-nm-thick polymer film. After the second parylene layer was peeled off with tape, the OECTs were ready for measurement. Electrical characterization of the devices was performed using a Keithley 4200 SCS analyser or an Fs-Pro semiconductor parameter analyser. An Ag/AgCl pellet (Warner Instruments) was employed as the gate electrode. The electrolyte was 0.1 M NaCl solution, which covered the polymer film in the channel. The film thickness was determined in a dry state with a profilometer (DEKTAK, Bruker).

Electromechanical coupling characterization of OECT materials

The device was constructed on a silica substrate with gold source and drain electrodes, as we did for the rigid OECT devices. No patterned encapsulation layer was applied. The width and length of the channel were 100 μm and 10 μm.

A P(bgTDPP-TVT-CN2)/chloroform solution (3–5 mg ml^{-1}) was spin-coated onto an octadecyltrimethoxysilane (OTS)-modified silica substrate in a nitrogen atmosphere. A 300-μm-thick free-standing

PDMS film was used to pick up the semiconducting polymer, which was stretched to a target strain and transferred to the silica substrate prepatterned with source and drain electrodes. The PDMS strip was carefully peeled off at 60 °C, leaving the stretched semiconducting polymer on the substrate. During the pickup, a high peeling rate was applied to the PDMS stamp to induce the rate-dependent delamination of the semiconducting film from the donor substrate. During printing, a lower peeling rate combined with mild heating enhanced adhesion to the receiving substrate, so that the film remained on the target surface while detaching from the PDMS stamp, thus completing the transfer. Excess polymer film outside the channel region was carefully wiped off using a wet Q-tip to reduce electrical leakage. After being covered with a 0.1 M NaCl aqueous solution electrolyte and an Ag/AgCl pellet gate electrode, the device was connected without a passivation layer to a semiconductor analyser for electrical characterization.

Mesoscale elastic OECT-based amplifier on a SEBS substrate

First, a SEBS H1221/toluene solution (120 mg ml^{-1}) was drop-cast onto an OTS-modified Si substrate. The wafer was carefully sealed to allow slow evaporation of the solvent overnight, thus forming a 400–1,000 μm SEBS elastic substrate. Then, the elastic substrate was pre-stretched and fixed. The SEBS film was stretched by 50% in the longitudinal direction and 20% in the perpendicular direction. Next, a shadow mask was attached to the pre-strained SEBS substrate, followed by thermal evaporation of 40 nm of gold at an evaporation rate of 0.5 Å s^{-1} (AMOD, Angstrom Engineering). After removing the shadow mask, stretchable source and drain electrodes were prepared. The device was then placed in a sealed oven with a 3 mM benzyl mercaptan/isopropyl alcohol solution for surface modification at 20 °C overnight. A P(bgTDPP-TVT-CN2) and P(g2T-T) film was spin-coated onto an OTS-modified Si slice and picked up by a small piece of PDMS film (10 mm × 2 mm). With a minimum resolution of 400 μm × 1,000 μm, it was aligned and transferred to the channel region, before or after the pre-strained substrate was released (Supplementary Figs. 24 and 25 and Supplementary Note 4).

To encapsulate the mesoscale elastic OECT-based amplifier, a PDMS solution (prepolymer with crosslinker 12:1 w/w, diluted by ethyl acetate 150 wt%) was carefully drop-cast onto the whole device, leaving the channel and contact pads exposed. The PDMS passive layer was then cured at 60 °C for 45 min in a glovebox for eventual crosslinking. The encapsulated device was then cut into strips to meet the needs of the application scenarios. FPCs and an anisotropic conducting film were used for the electrical interconnections. The bonding of the anisotropic conducting film was performed using a constant-temperature hot press machine (GZC-COF280, Hailunda Technology) at 0.01 MPa and 100 °C for 1 min to establish an electrical connection between the elastic amplifier and the FPC. Finally, a zero-insertion-force socket was used to connect the FPC to a semiconductor analyser for the electrical characterization.

Mesoscale flexible OECT-based amplifier on a PI substrate

The mesoscale flexible OECT-based amplifier was fabricated on a 25-μm PI substrate, using a similar fabrication process used for the mesoscale elastic OECT-based amplifier with necessary adjustments. First, Ti (5 nm) and Au (40 nm) were magnetron-sputtered through a shadow mask onto a clean PI substrate. The whole device was then exposed to a benzyl mercaptan atmosphere for surface modification as described above. Later, the p- and n-type semiconductor polymers were transferred to the channel part. Finally, another layer of PI with an adhesion agent was laminated onto the metal electrode as an encapsulation layer, while leaving the channel exposed to the electrolyte.

Microscale elastic OECT-based amplifier

A 3% poly(vinyl alcohol) (PVA) aqueous solution was spin-coated onto a clean silica wafer at 1,000 rpm to form a releasing layer. The edge of the PVA was wiped with wet Q-tips to avoid delamination during fabrication. A SEBS H1221/toluene solution (120 mg ml^{-1}) was drop-cast onto the substrate. After slow evaporation of the solvent overnight, a 400–1,000 μm elastic substrate was prepared. Then, a 40-nm gold layer was thermally evaporated onto the SEBS. Photoresist S1813 was spin-coated and baked with slow heating and annealing rates to avoid crack formation. Then the photoresist was patterned by lithography (MA6, SUSS), and the exposed gold was wet-etched by an Au etchant (120 mM KI/32 mM I_2 in DI water) for 3 min. The etchant was thoroughly washed off with DI water. The residual photoresist was dissolved in acetone and isopropyl alcohol, followed by nitrogen drying. Next, a P(g2T-T)/hexafluoroisopropanol (HFIP) solution of 3 mg ml^{-1} was spin-coated onto the substrate at 1,000 rpm, which was followed by a layer of fluoropolymer (Novec 2702, 3M) as protective layer I. A 50-nm layer of Cu was magnetron-sputtered as protective layer II. Photoresist AZ10XT was spin-coated and patterned to cover the channel part of the device. Protective layer II was etched with a Cu etchant. Protective layer I and p-type polymer were dry-etched by reactive-ion etching loaded with O_2 and CF_4. Isopropyl alcohol was used to dissolve and wash away the excess AZ10XT, which completed the patterning of the p-type OECT material. An n-type layer of P(bgTDPP-TVT-CN2) was then spin-coated and patterned by dry-etching under the protection of the fluoropolymer and photoresist, using a similar fluoropolymer protection method as described above. Finally, the fluoropolymer was dissolved by a fluorinated solvent, and the Cu protection layer was lifted off, leaving both the p- and n-type semiconducting films on the channel. The films had a size of 100 μm × 10 μm. The device was ready for characterization without passive layers.

Tensile tests

Tensile tests under monotonic and cyclic loading conditions were conducted using a low-force testing system (68SC-05, Instron), with devices fixed to the clamps. Specifically, devices with PI and SEBS substrates were monotonically stretched at a loading rate of 5 mm min^{-1}, and elastic devices were also subjected to cyclic tensile tests (continuous loading and unloading) at a rate of 20 mm min^{-1}.

Long-term immersion stability test

The elastic devices were first bonded with an FPC connecting wire, and the welding joint was encapsulated for waterproofing. The as-fabricated device was then soaked in rabbit plasma (R774419, Aladdin) or PBS solution for ageing. At certain time intervals, the device was taken out, dried and its electronic properties were measured using a drop of 0.1 M NaCl solution as the electrolyte. After each measurement, the device was re-immersed in the solution to continue the long-term ageing. Details of the experimental set-up are provided in Fig. 4c and Supplementary Fig. 32.

Cytotoxicity

The polymer P(bgTDPP-TVT-CN2) was dissolved in chloroform and spin-coated onto glass substrates, baked at 100 °C, washed with DI water and blow-dried. After a brief oxygen plasma treatment, samples were placed into 12-well plates. Mouse fibroblasts (NIH-3T3, Cellcook) were then seeded into each well. Cells were cultured in high-glucose DMEM (CM2016, CellCook) supplemented with 10% fetal bovine serum (BL201A, Biosharp), 100 U ml^{-1} penicillin and 100 U ml^{-1} streptomycin (SV30010, HyClone) at 37 °C in a humidified atmosphere with 5% CO_2. After 24 h of incubation, live/dead staining (E-CK-A354, Elabscience) was performed. Briefly, cells were washed with PBS, and a working solution was prepared by adding 1 μM calcein-AM and 7.5 μM propidium iodide to DMEM. The working solution was added to the cultures and incubated at 37 °C for 30 min. Live cells (green fluorescence) and dead cells (red fluorescence) were then observed using a microscope (Eclipse LV100ND POL/DS, Nikon) equipped with a light source (C-HGFI, Nikon) and a 490-nm excitation filter.

For the MTT assay, the P(bgTDPP-TVT-CN2)/chloroform solution was first drop-cast onto OTS-modified silica wafers, vacuum-treated

for 12 h after peeling and then washed with DI water, PBS and DMEM (CM2016, CellCook). The samples were then incubated in complete culture medium (0.8 mg ml^{-1}) at 37 °C for 24 h. The extracts were filtered through a 0.22-μm filter and diluted to the desired concentrations. NIH-3T3 cells were then seeded into 96-well plates (2×10^4 cells per well) and incubated for 24 h. After incubation, the cells were washed with PBS and treated with extraction media of different concentrations for another 24 h. The extract was then removed, and MTT solution (0.5 mg ml^{-1} in DMEM, MA0198, MeilunBio) was added. Following incubation for 4 h in the dark, the solution was carefully removed, and 100 μl of dimethyl sulfoxide was added to each well to dissolve the formazan crystals. The absorbance was measured at 570 nm using a microplate reader (Multiskan FC, Thermo Scientific).

Histological processing for haematoxylin and eosin, Masson's trichrome and immunofluorescence staining

After anaesthetizing the Sprague Dawley rats (aged 10–12 weeks) with isoflurane (R510-22-10, RWD Life Science Co), we subcutaneously implanted the elastic amplifier device ($10 \times 6 \times 0.4$ mm^3) and the PI-based device ($10 \times 6 \times 0.025$ mm^3) into the hindlimb tissue of the rats. The wound was closed with sutures. After 6 weeks, the rats were euthanized, and the implanted devices, along with the surrounding tissue, were excised and fixed in 4% paraformaldehyde (BL539A 4%, Biosharp) for 24 h. The samples were then dehydrated and embedded in paraffin, and pathological sections were prepared. The sections were deparaffinized sequentially with xylene, ethanol and distilled water. Samples were stained with haematoxylin and eosin (QY1013, Shanghai Qianya Jinzhi Biotechnology) and Masson's trichrome staining kits (QY1018, Shanghai Qianya Jinzhi Biotechnology). They were then washed with xylene and mounted with neutral resin. The entire sections were imaged using a microscope (DM2500, Leica). Immunofluorescence staining was performed as follows. After blocking endogenous peroxidase and nonspecific sites, sections were incubated with the primary antibodies (α-SMA, a myofibroblast marker, green, and CD68, a macrophage marker, red) overnight at 4 °C, followed by incubation with the secondary antibodies and tyramide signal amplification for 10 min, using specified fluorescence channels. For multiplex labelling, antibody elution and sequential staining cycles were performed. Nuclei were counterstained with DAPI (4',6-diamidino-2-phenylindole), and sections were mounted with antifade medium for imaging. The primary antibodies were anti-alpha smooth muscle actin (α-SMA) antibody (ab7817, Abcam; dilution 1:2,000) and anti-CD68 antibody (ab283654, Abcam; dilution 1:500). The secondary antibodies were goat anti-rabbit IgG H&L (HRP) (ab205718, Abcam; dilution 1:5,000) and goat anti-mouse IgG H&L (HRP) (ab205719, Abcam; dilution: 1:5,000).

In vivo ECG recording

All animal experiments were approved by the ethics committee (Protocol No. DLASBD0683, approved by the Institutional Animal Care and Use Committee of Peking University Health Science Center) and conducted in compliance with guidelines for animal experimentation.

Female Sprague Dawley rats aged 10–12 weeks from the Department of Laboratory Animal Science, Peking University Health Science Center, were used in the acute epicardial recording experiments. Rats were anaesthetized with isoflurane (2–5% in oxygen) for general anaesthesia. An acute tracheotomy was conducted, and the rats were intubated on a ventilator (VentStar Small Animal Ventilator, RWD Life Science). The ribs were cut to expose the heart, and the pericardium was gently removed. During ECG recording, working and reference electrodes were lightly placed on the heart tissue and recorded with an Fs-Pro semiconductor parameter analyser with a 1,000-Hz sampling rate. The device could lightly cover and become attached to the epicardial surface due to its softness and the modest adhesion of SEBS. By adjusting the supply voltage (V_{DD} = 0.25 V and V_{SS} = −0.65 V), the amplifier input could be fixed at zero bias. The animal was directly grounded by a commercial AgCl gel electrode (3M) attached to the abdominal region. The recorded signals were digitally filtered using a notch filter of 50 Hz. Then, a digital high-pass filter of 10 Hz was used to focus on the ECG frequency band. Letswave7 MATLAB toolbox was used to plot the ECG time–frequency domain analysis diagrams.

Female Japanese white rabbits (aged 6-7 months, weighing 2.5 kg) from the Department of Laboratory Animal Science, Peking University Health Science Center, were selected for this study. After anaesthesia, the rabbit's heart was exposed via median sternotomy. The amplifier and reference electrode were used to record the ECG signal, like the method we used for the rat experiment. At the end of the study, the animal was euthanized humanely with the air embolism method.

Statistics and reproducibility

All experiments were independently repeated at least three times. The number of independent experiments *n* is specified in the figure captions. Imaging experiments, including optical and electron microscopy, were independently repeated at least five times with similar results; representative images are shown.

Ethics and inclusion statement

Collaborators agreed on roles and responsibilities ahead of the research and discussed any capacity-building plans for local researchers. Animal experiments were approved by the Institutional Animal Care and Use Committee of Peking University Health Science Center and were conducted in compliance with guidelines for animal experimentation.

Reporting summary

Further information on research design is available in the Nature Portfolio Reporting Summary linked to this article.

Data availability

All data supporting the findings of this study are available in the main text or the Supplementary Information. Other related raw data are fully and freely available from the corresponding authors. Source data are provided with this paper.

Code availability

No central code was developed for this work.

References

1. Rivnay, J., Owens, R. M. & Malliaras, G. G. The rise of organic bioelectronics. *Chem. Mater.* **26**, 679–685 (2014).
2. Li, Y., Li, N., De Oliveira, N. & Wang, S. Implantable bioelectronics toward long-term stability and sustainability. *Matter* **4**, 1125–1141 (2021).
3. Zhao, C., Park, J., Root, S. E. & Bao, Z. Skin-inspired soft bioelectronic materials, devices and systems. *Nat. Rev. Bioeng.* **2**, 671–690 (2024).
4. Oldroyd, P. & Malliaras, G. G. Achieving long-term stability of thin-film electrodes for neurostimulation. *Acta Biomater.* **139**, 65–81 (2022).
5. Hong, G. & Lieber, C. M. Novel electrode technologies for neural recordings. *Nat. Rev. Neurosci.* **20**, 330–345 (2019).
6. Minev, I. R. et al. Electronic dura mater for long-term multimodal neural interfaces. *Science* **347**, 159–163 (2015).
7. Lu, B. et al. Pure PEDOT:PSS hydrogels. *Nat. Commun.* **10**, 1043 (2019).
8. Tringides, C. M. et al. Viscoelastic surface electrode arrays to interface with viscoelastic tissues. *Nat. Nanotechnol.* **16**, 1019–1029 (2021).
9. Jiang, Z. et al. A 1.3-micrometre-thick elastic conductor for seamless on-skin and implantable sensors. *Nat. Electron.* **5**, 784–793 (2022).

10. Sharafkhani, N. et al. Neural tissue-microelectrode interaction: brain micromotion, electrical impedance, and flexible microelectrode insertion. *J. Neurosci. Methods* **365**, 109388 (2022).
11. Li, P. et al. N-type semiconducting hydrogel. *Science* **384**, 557–563 (2024).
12. Wang, W. et al. Neuromorphic sensorimotor loop embodied by monolithically integrated, low-voltage, soft e-skin. *Science* **380**, 735–742 (2023).
13. Zhong, D. et al. High-speed and large-scale intrinsically stretchable integrated circuits. *Nature* **627**, 313–320 (2024).
14. Wang, W. et al. Strain-insensitive intrinsically stretchable transistors and circuits. *Nat. Electron.* **4**, 143–150 (2021).
15. Venkatraman, V. et al. Subthreshold operation of organic electrochemical transistors for biosignal amplification. *Adv. Sci.* **5**, 1800453 (2018).
16. Huang, W. et al. Vertical organic electrochemical transistors for complementary circuits. *Nature* **613**, 496–502 (2023).
17. Nawaz, A., Liu, Q., Leong, W. L., Fairfull-Smith, K. E. & Sonar, P. Organic electrochemical transistors for in vivo bioelectronics. *Adv. Mater.* **33**, 2101874 (2021).
18. Wu, M. et al. Ultrathin, soft, bioresorbable organic electrochemical transistors for transient spatiotemporal mapping of brain activity. *Adv. Sci.* **10**, 2300504 (2023).
19. Dai, Y. H. et al. Stretchable redox-active semiconducting polymers for high-performance organic electrochemical transistors. *Adv. Mater.* **34**, 2201178 (2022).
20. Chen, J. et al. Highly stretchable organic electrochemical transistors with strain-resistant performance. *Nat. Mater.* **21**, 564–571 (2022).
21. Li, N. et al. Bioadhesive polymer semiconductors and transistors for intimate biointerfaces. *Science* **381**, 686–693 (2023).
22. Braendlein, M., Lonjaret, T., Leleux, P., Badier, J. & Malliaras, G. G. Voltage amplifier based on organic electrochemical transistor. *Adv. Sci.* **4**, 1600247 (2017).
23. Uguz, I. et al. Complementary integration of organic electrochemical transistors for front-end amplifier circuits of flexible neural implants. *Sci. Adv.* **10**, eadi9710 (2024).
24. Kim, J. et al. Monolithically integrated high-density vertical organic electrochemical transistor arrays and complementary circuits. *Nat. Electron.* **7**, 234–243 (2024).
25. Gao, D. & Fabiano, S. Conductive hydrogels put electrons in charge. *Science* **384**, 509–510 (2024).
26. Su, X. et al. A highly conducting polymer for self-healable, printable, and stretchable organic electrochemical transistor arrays and near hysteresis-free soft tactile sensors. *Adv. Mater.* **34**, 2200682 (2022).
27. Dai, S. et al. Intrinsically stretchable neuromorphic devices for on-body processing of health data with artificial intelligence. *Matter* **5**, 3375–3390 (2022).
28. Liu, D. et al. A wearable in-sensor computing platform based on stretchable organic electrochemical transistors. *Nat. Electron.* **7**, 1176–1185 (2024).
29. Dai, Y. et al. Soft hydrogel semiconductors with augmented biointeractive functions. *Science* **386**, 431–439 (2024).
30. Liu, Q., Bottle, S. E. & Sonar, P. Developments of diketopyrrolopyrrole-dye-based organic semiconductors for a wide range of applications in electronics. *Adv. Mater.* **32**, 1903882 (2020).
31. Zhang, L. et al. Achieving the high charge mobility of conjugated polymers under cyclic stretching by changing the interaction parameter between solvent and sidechain. *Polymer* **275**, 125912 (2023).
32. Li, P., Shi, J., Lei, Y., Huang, Z. & Lei, T. Switching p-type to high-performance n-type organic electrochemical transistors via doped state engineering. *Nat. Commun.* **13**, 5970 (2022).
33. Shi, J. et al. Revealing the role of polaron distribution on the performance of n-type organic electrochemical transistors. *Chem. Mater.* **34**, 864–872 (2022).
34. Jia, H. et al. Engineering donor–acceptor conjugated polymers for high-performance and fast-response organic electrochemical transistors. *J. Mater. Chem. C* **9**, 4927–4934 (2021).
35. Mun, J. et al. A design strategy for high mobility stretchable polymer semiconductors. *Nat. Commun.* **12**, 3572 (2021).
36. Wang, Z. et al. Aggregation structure and glass transition of intrinsically stretchable semiconducting polymers. *Matter* **6**, 3434–3448 (2023).
37. Khodagholy, D. et al. High transconductance organic electrochemical transistors. *Nat. Commun.* **4**, 2133 (2013).
38. Inal, S., Malliaras, G. G. & Rivnay, J. Benchmarking organic mixed conductors for transistors. *Nat. Commun.* **8**, 1767 (2017).
39. Zhang, C. et al. Polythiophenes for high-performance n-type organic electrochemical transistors. *Adv. Funct. Mater.* **35**, 2419706 (2025).
40. Yan, X. et al. Approaching disorder-tolerant semiconducting polymers. *Nat. Commun.* **12**, 5723 (2021).
41. Wu, H.-C. et al. Highly stretchable polymer semiconductor thin films with multi-modal energy dissipation and high relative stretchability. *Nat. Commun.* **14**, 8382 (2023).
42. Zhao, C. et al. Skin-like drift-free biosensors with stretchable diode-connected organic field-effect transistors. *Nat. Electron.* **8**, 981–993 (2025).
43. Dai, S. et al. Vertical-structure overcomes the strain limit of stretchable organic electrochemical transistors. *Adv. Mater.* **37**, 2413951 (2024).
44. Hou, S. et al. Stretchable electronics with strain-resistive performance. *Small* **20**, 2306749 (2024).
45. Vo, N. T. P. et al. Autonomous self-healing supramolecular polymer transistors for skin electronics. *Nat. Commun.* **15**, 3433 (2024).
46. Guan, Y.-S. et al. Elastic electronics based on micromesh-structured rubbery semiconductor films. *Nat. Electron.* **5**, 881–892 (2022).
47. Wang, S. et al. Skin electronics from scalable fabrication of an intrinsically stretchable transistor array. *Nature* **555**, 83–88 (2018).
48. Cea, C. et al. Integrated internal ion-gated organic electrochemical transistors for stand-alone conformable bioelectronics. *Nat. Mater.* **22**, 1227–1235 (2023).
49. Yoon, J. et al. Fabrication of stretchable single-walled carbon nanotube logic devices. *Small* **10**, 2910–2917 (2014).
50. Yang, F., Liu, S., Li, C. & Lv, A. High-performance organic field-effect transistors and inverters with good flexibility and low operating voltage. *ChemPhysChem* **26**, e202300683 (2025).

Acknowledgements

We acknowledge the Molecular Materials and Nanofabrication Laboratory, the Materials Processing and Analysis Center and the Electron Microscopy Laboratory of Peking University for instrument use. The computational work was supported by the High-Performance Computing Platform of Peking University. We thank beamline BL14B1 (Shanghai Synchrotron Radiation Facility) for providing beam time for part of the X-ray scattering measurement. We acknowledge Peking University Third Hospital for animal experiments.

Author contributions

W.S., X.P. and T.L. conceived the idea and designed the experiments. X.P. synthesized the n-type polymer. W.S. and X.P. performed the calculations and structural characterization of the polymer. X.L. provided the p-type polymer. W.S., P.L., B.W. and C.W. performed the electrical characterization of the polymer and fabricated the elastic devices. X.-Y.Z. and W.S. performed the

polarized UV-vis-NIR spectroscopy test. S.L. and X.W. performed the tensile test. K.L. performed the contact angle test. Y.W. and P.G. performed the AFM measurements. W.S., W.X., W.Y., Y.Z., B.Y. and H.O. performed the cytotoxicity and in vivo animal experiments. W.S. and C.Z. performed the acquisition and analysis of signals. W.S., X.P., Z.Z. and T.L. wrote the paper. All authors reviewed and edited the article.

Funding

T.L. discloses support for the research of this work from the National Natural Science Foundation of China (T2425010, T2521001). Z.Z. discloses support for publication of this work from the National Natural Science Foundation of China (5243219), the Beijing Natural Science Foundation (2262050) and the Fundamental Research Funds for the Central Universities, Peking University (PKU2026PKULCXQ023). W.Y. discloses support for the research of this work from the Peking University Third Hospital Fund for Interdisciplinary Research (BYSYJC2025063). H.O. discloses support for publication of this work from the Beijing Natural Science Foundation (L252150) and Peking University Third Hospital Innovation and Transformation Fund (BYSYZHKC202506). The other authors received no specific funding for this work.

Competing interests

The authors declare no competing interests.

Additional information

Supplementary information The online version contains supplementary material available at https://doi.org/10.1038/s44460-026-00091-7.

Correspondence and requests for materials should be addressed to Zhi Zhang or Ting Lei.

Peer review information *Nature Sensors* thanks Wei Huang, Sahika Inal and Sihong Wang for their contribution to the peer review of this work. Peer reviewer reports are available.

nature portfolio

Corresponding author(s): Ting Lei

Last updated by author(s): Apr 27, 2026

Reporting Summary

Nature Portfolio wishes to improve the reproducibility of the work that we publish. This form provides structure for consistency and transparency in reporting. For further information on Nature Portfolio policies, see our Editorial Policies and the Editorial Policy Checklist.

Statistics

For all statistical analyses, confirm that the following items are present in the figure legend, table legend, main text, or Methods section.

n/a	Confirmed
☐	☒ The exact sample size (*n*) for each experimental group/condition, given as a discrete number and unit of measurement
☐	☒ A statement on whether measurements were taken from distinct samples or whether the same sample was measured repeatedly
☒	☐ The statistical test(s) used AND whether they are one- or two-sided *Only common tests should be described solely by name; describe more complex techniques in the Methods section.*
☒	☐ A description of all covariates tested
☐	☒ A description of any assumptions or corrections, such as tests of normality and adjustment for multiple comparisons
☐	☒ A full description of the statistical parameters including central tendency (e.g. means) or other basic estimates (e.g. regression coefficient) AND variation (e.g. standard deviation) or associated estimates of uncertainty (e.g. confidence intervals)
☒	☐ For null hypothesis testing, the test statistic (e.g. *F*, *t*, *r*) with confidence intervals, effect sizes, degrees of freedom and *P* value noted *Give P values as exact values whenever suitable.*
☒	☐ For Bayesian analysis, information on the choice of priors and Markov chain Monte Carlo settings
☒	☐ For hierarchical and complex designs, identification of the appropriate level for tests and full reporting of outcomes
☒	☐ Estimates of effect sizes (e.g. Cohen's *d*, Pearson's *r*), indicating how they were calculated

Our web collection on statistics for biologists contains articles on many of the points above.

Software and code

Policy information about availability of computer code

Data collection	LabExpress in Fs-Pro semiconductor parameter analyzer (PDA): OECT and inverter characterization, ECoG recording; EC-Lab(V11.52): electrochemical measurements; Fiji-ImageJ: fluorescence quantification
Data analysis	The electrophysiological signals were analyzed by Signal Processing Function in Origin 2023b, and MATLAB(R2025a) with toolbox letswave7. The Atomic force microscopy (AFM) modulus measurements data were processed and analyzed using Nanoscope Analysis software V1.4 (Bruker). Data processing of 2D-GIWAXS measurements was performed using Igor Pro 9 software with the Nika and WAXTools packages. Histological analyses were performed using CaseViewer 2.4. Geometry optimization and relaxed potential energy surface scans were performed using Gaussian 16 and Gauss View 6.

For manuscripts utilizing custom algorithms or software that are central to the research but not yet described in published literature, software must be made available to editors and reviewers. We strongly encourage code deposition in a community repository (e.g. GitHub). See the Nature Portfolio guidelines for submitting code & software for further information.

Data

Policy information about availability of data

All manuscripts must include a data availability statement. This statement should provide the following information, where applicable:

- Accession codes, unique identifiers, or web links for publicly available datasets
- A description of any restrictions on data availability
- For clinical datasets or third party data, please ensure that the statement adheres to our policy

All data supporting the findings of this study are available in the paper and its Supplementary Information. Other related raw data are fully and freely available from the corresponding author at the point of publication. Source data are provided with this paper.

Research involving human participants, their data, or biological material

Policy information about studies with human participants or human data. See also policy information about sex, gender (identity/presentation), and sexual orientation and race, ethnicity and racism.

Reporting on sex and gender	n/a
Reporting on race, ethnicity, or other socially relevant groupings	n/a
Population characteristics	n/a
Recruitment	n/a
Ethics oversight	n/a

Note that full information on the approval of the study protocol must also be provided in the manuscript.

Field-specific reporting

Please select the one below that is the best fit for your research. If you are not sure, read the appropriate sections before making your selection.

☒ Life sciences ☐ Behavioural & social sciences ☐ Ecological, evolutionary & environmental sciences

For a reference copy of the document with all sections, see nature.com/documents/nr-reporting-summary-flat.pdf

Life sciences study design

All studies must disclose on these points even when the disclosure is negative.

Sample size	To evaluate the electrophysiological signal acquisition performance of the proposed device while adhering to the 3R principles of animal ethics (Replacement, Reduction, and Refinement), we conducted experiments using two rats and one rabbit. Sample sizes were chosen based on previous studies in the field and are consistent with commonly used practices for device characterization and in vivo electrophysiological experiments.
Data exclusions	Parts of in vivo electrocardiosignals were excluded. Since this electrophysiological signal exhibits periodicity, a short segment (e.g., a few seconds) is sufficient to characterize the complete signal. The applied exclusion criteria adhered to established clinical research standards. Data were excluded when clear experimental artefacts were identified (e.g., device failure or measurement errors), according to pre-established criteria.
Replication	The interval between each independent experiment was at least one week. All experiments were repeated on independent devices or samples, and consistent results were obtained, confirming the reproducibility of the findings.
Randomization	For the animal experiments, only species-level specifications were provided by the authors, with individual subjects randomly assigned by the Institutional Animal Care and Use Committee of Peking University Health Science Center.
Blinding	Blinding was not relevant to this study, as the experiments involved objective device measurements and signal recordings without subjective assessment.

Reporting for specific materials, systems and methods

We require information from authors about some types of materials, experimental systems and methods used in many studies. Here, indicate whether each material, system or method listed is relevant to your study. If you are not sure if a list item applies to your research, read the appropriate section before selecting a response.

Materials & experimental systems

n/a	Involved in the study
☐	☒ Antibodies
☐	☒ Eukaryotic cell lines
☒	☐ Palaeontology and archaeology
☐	☒ Animals and other organisms
☒	☐ Clinical data
☒	☐ Dual use research of concern
☒	☐ Plants

Methods

n/a	Involved in the study
☒	☐ ChIP-seq
☒	☐ Flow cytometry
☒	☐ MRI-based neuroimaging

Antibodies

Antibodies used

Primary antibodies: Anti-alpha smooth muscle Actin antibody (ab7817, abcam; dilution: 1:2000), Anti-CD68 antibody (ab283654, abcam; dilution: 1:500);
Secondary antibodies: Goat anti-rabbit IgG H&L (HRP) (ab205718, abcam; dilution: 1:5000), Goat anti-mouse IgG H&L (HRP) (ab205719, abcam; dilution: 1:5000)

Validation

Each primary antibody used in this study was validated for the relevant species and application. Validation information was obtained from the manufacturers' datasheets, which specify species reactivity and application suitability.
Validation statement on the manufacturer's website and citations:
https://www.abcam.cn/products/primary-antibodies/alpha-smooth-muscle-actin-antibody-1a4-ab7817
https://www.abcam.cn/products/primary-antibodies/cd68-antibody-epr23917-164-ab283654
https://www.abcam.cn/products/secondary-antibodies/goat-rabbit-igg-h-l-hrp-ab205718
https://www.abcam.cn/products/secondary-antibodies/goat-mouse-igg-h-l-hrp-ab205719

Eukaryotic cell lines

Policy information about cell lines and Sex and Gender in Research

Cell line source(s)

The NIH-3T3 cell line (mouse embryonic fibroblast) was obtained from Cellcook. This cell line is derived from mouse and therefore sex is not applicable.

Authentication

The NIH-3T3 cell line was not further authenticated.

Mycoplasma contamination

The cell lines were not tested for mycoplasma contamination.

Commonly misidentified lines
(See ICLAC register)

The NIH-3T3 cell line is not listed among commonly misidentified cell lines.

Animals and other research organisms

Policy information about studies involving animals; ARRIVE guidelines recommended for reporting animal research, and Sex and Gender in Research

Laboratory animals

The study involved SD rats aged 10–12 weeks and adult Japanese White Rabbit (2.5 kg) aged 6-7 months. All animals were obtained from the Department of Laboratory Animal Science, Peking University Health Science Center.

Wild animals

The study did not involve wild animals.

Reporting on sex

Only female animals were used in this study. Sex was not considered as a variable in the experimental design, as no sex-dependent effects were expected.

Field-collected samples

The study did not involve samples collected from the field.

Ethics oversight

All animal experiments were conducted in accordance with institutional guidelines and were approved by by the Institutional Animal Care and Use Committee of Peking University Health Science Center (protocol No. DLASBD0683)

Note that full information on the approval of the study protocol must also be provided in the manuscript.

Plants

Seed stocks

This study did not involve plants.

Novel plant genotypes

Describe the methods by which all novel plant genotypes were produced. This includes those generated by transgenic approaches, gene editing, chemical/radiation-based mutagenesis and hybridization. For transgenic lines, describe the transformation method, the number of independent lines analyzed and the generation upon which experiments were performed. For gene-edited lines, describe the editor used, the endogenous sequence targeted for editing, the targeting guide RNA sequence (if applicable) and how the editor was applied.

Authentication

Describe any authentication procedures for each seed stock used or novel genotype generated. Describe any experiments used to assess the effect of a mutation and, where applicable, how potential secondary effects (e.g. second site T-DNA insertions, mosiacism, off-target gene editing) were examined.